



An effective approach to improve electrochemical performance of thick electrodes

Kaifang Song^{1,2} · Wenjie Li¹ · Zhan Chen¹ · Xiangkun Wu¹ · Qian Zhou³ · Kent Snyder³ · Lan Zhang^{1,2}

Received: 10 August 2020 / Revised: 18 November 2020 / Accepted: 12 January 2021 / Published online: 19 January 2021

© The Author(s), under exclusive licence to Springer-Verlag GmbH, DE part of Springer Nature 2021

Abstract

Increasing areal active material loading by thick electrodes is a direct and effective approach to improve the energy density of lithium-ion batteries (LIBs). However, it may also induce large polarization effects and reduce the active material utilization, especially under high charge/discharge current densities. In this work, dual-layered $\text{LiNi}_{0.8}\text{Co}_{0.15}\text{Al}_{0.05}\text{O}_2$ (NCA) cathodes with high areal capacity of about 5 mAh/cm^2 and gradient porosity are prepared via a layer-by-layer method, in which carbon nanotubes (CNTs) and Super P (SP) carbon are used to build the electron conducting networks as well as to adjust the porosity. It is demonstrated that the CNT-SP cathode, which uses CNTs as the conductive agent in the lower layer (close to the current collector) and SP as the conductive agent in the upper layer (close to the separator), provides the highest areal capacity of 4.81 mAh/cm^2 among all configurations studied (CNT-SP, SP-SP, SP-CNT, and CNT-CNT). And it exhibits high capacity retention of 99.5% over 100 cycles in NCA||graphite full pouch cells at current density of 0.2 C rate. The excellent performance of the thick CNT-SP cathode is attributed to the construction of favorable conductive networks which can provide effective and reliable paths for electron transport and Li^+ diffusion. Moreover, a thinner electrode/electrolyte interphase layer is found to form in the CNT-SP electrode. This research reveals a viable approach for ameliorating the significant polarization effects and limited active material utilization in thick electrodes through alternate configurations of the conductive agents, which can be easily adopted in state-of-the-art battery manufacturing processes.

Keywords Lithium-ion battery · Dual-layered structure · Conductive agent · Areal loading · Thick electrode

Introduction

Lithium-ion batteries (LIBs) are widely used in consumer electronics and electric vehicles (EVs), as well as in energy storage applications due to their long cycle life, wide operating temperature range, as well as high energy and power density [1–6]. Towards meeting the requirement of EV customers to provide

longer driving range per charge, enhancing the energy density of LIBs is an unavoidable trend. One of the general approaches to improve the energy density is via increasing the areal active material loading through the use of thicker electrodes, thereby decreasing the weight fraction of inactive components (current collectors, separator, and electrolyte, etc.) [7–12]. Typically, if we can increase the areal capacity to 5 mAh/cm^2 (it is about 3 mAh/cm^2 in state-of-the-art LIBs), energy density of the cell could be enhanced approximately by 10% [13]. However, simply increasing electrode thickness would otherwise increase the transport distance for both ions and electrons, leading to severe polarization and poor electrochemical performance, especially at high current densities. Constructing adequate Li^+ diffusion paths and electron conductive networks are the key challenges in achieving beneficial thick porous electrode performance [14, 15].

Modification of porosity and pore structure are the most effective ways to regulate Li^+ transport. However, significant experimental or engineering efforts are typically required to optimize the impact of these parameters in concert with the impact of other factors, such as negative/positive electrode

✉ Xiangkun Wu
xkwu@ipe.ac.cn

✉ Lan Zhang
zhangl@ipe.ac.cn

¹ Beijing Key Laboratory of Ionic Liquids Clean Process, Key Laboratory of Green Process and Engineering, Institute of Process Engineering, Chinese Academy of Sciences, Beijing 100190, China

² University of the Chinese Academy of Sciences, Beijing 100049, China

³ Electrification Subsystems & Power Supply, Ford Motor Company, Dearborn, MI 48121, USA

capacity ratio, electrolyte volume, and others, in order to achieve improved overall battery performance. To consider overall optimization and reduce the required experimental effort, mathematical models have been used and have become powerful tools to guide electrode design [16–18]. Srinivasan and Newman [18] simulated the performance of natural graphite/LiFePO₄ (LFP) batteries with various cathode structure designs, and they found that a thinner electrode with higher porosity was preferable for faster discharge due to the improved ion transport dynamics, although it was conversely unfavorable in terms of energy density. Cho's [19] group investigated the influence of porosity on ion transport in LFP electrodes by simulation and experiment, with both methods of investigation showing that the ionic transport would be largely limited when the porosity was less than 0.3. Considering the Li⁺ concentration gradient in thick electrodes [20], researchers started to design and develop electrodes with regulated pore structures [21–23]. With the aid of a dual-scale porosity structure extending through the active material thickness of the electrode, Chiang's group made LiCoO₂ (LCO) electrodes with areal capacity higher than 9 mAh/cm² (0.5 C rate) [21]. Bitsch et al. found that staged porosity perpendicular to the current collector was favorable for enhancing Li⁺ transport in graphite electrodes [24]. Moreover, the structure could be easily obtained by proportionally adding octanol during the electrode slurry preparation. Nevertheless, there appears to be relatively less investigation of this type of approach in the literature with the use of Ni-rich high capacity cathode materials such as Li(Ni_{0.8}Co_{0.15}Al_{0.05})O₂ (NCA) or Li(Ni_{0.8}Co_{0.1}Mn_{0.1})O₂ (NCM811). Unlike LFP and LCO, Ni-rich materials under high states of charge (SoC) are much more oxidatively unstable so that a cathode/electrolyte interphase (CEI) is essential [25]. Moreover, the crosstalk between cathode and anode may also influence the battery performance [26] so that related mathematical models may become less reliable. In this article, we prepared dual-layered NCA electrodes with gradient porosity through the use of various conductive networks and created via a layer-by-layer coating method to investigate the influence of electrode microstructures on the battery electrochemical performance. Two typical conductive agents (CAs), Super P (SP) and carbon nanotubes (CNTs), were used in the cathode preparations. Each agent was adopted in one layer of the cathode to form the conductive network as well as regulate the porosity. It was shown that the CNT-SP cathode that contained CNTs in the lower layer (close to the current collector) and SP in the upper layer (close to the separator) exhibited the highest porosity in the lower layer and the lowest porosity in the upper layer, and demonstrated the best performance among the 4 types of as-prepared electrodes (CNT-SP, CNT-CNT, SP-SP, SP-CNT). Electrochemical impedance tests showed that all the electrodes deliver high areal capacity of about 5 mAh/cm², and the NCA||graphite cell with CNT-SP cathode exhibited the

lowest resistance. Post mortem XPS analysis verified that thinner CEI films formed on the surface of CNT-SP cathodes, which indicated that parasitic reactions were reduced at these electrode surfaces.

Experimental

Electrode preparation and cell assembly

The positive slurry was prepared by mixing 97 wt% NCA (JFE, Japan), 2 wt% polyvinylidene fluoride (PVDF, Solvay Solef 5130, USA), and 1 wt% CAs with *N*-methyl pyrrolidone (NMP, Sinopharm Chemical Reagent Co., Ltd., China) in a vacuum agitator. The solid content was controlled to 65 wt%. The slurry was further treated by a high speed disperser (FM40L, PRIMIX Corporation, Japan) to ensure uniform dispersion. The dual-layer electrodes were prepared by a two-step coating method. Firstly, the slurry was evenly coated on aluminum foil by a pilot-scale transfer roll coater (Dongguan Areconn Precision Machinery Co., Ltd., China) with three different drying zones (the temperature was set at 85, 90, and 92 °C, respectively) and a total length of 6 m. The coating speed was set at 2 m/min to assure complete drying. The subsequent coating (thickness ~ 150 μm) was applied on the previously coated and dried electrode using an automatic doctor blade coating machine (MSK-AFA-SC200, Shenzhen Kejing Star Technology Co., Ltd., China). And then the electrodes were dried under 80 °C in an oven. After drying, the dual-layered electrode was compacted by a rolling machine (MSK-2150, Shenzhen Kejing Star Technology Co., Ltd., China) resulting in a compaction density of about 3.55 g/cm³. The overall design areal active material loading and capacity of the positive electrode was approximately 27.2 mg/cm² and 5 mAh/cm², respectively. Four kinds of positive electrodes were fabricated according to the CA in each layer. The most common CAs used in the state-of-the-art battery industry, SP and CNTs, were chosen to be studied in this work. These CAs provided point-to-point and point-to-line electron conduction pathways, respectively [27].

The cathode with CNTs (Jiangsu Cnano Technology Co., Ltd., China) in the lower layer (close to the current collector) and SP (Imerys Graphite & Carbon Switzerland S.a.Ltd., UK) in the upper layer (close to the separator) was named as CNT-SP. Similarly, the other three kinds of electrodes were labeled as SP-CNT, SP-SP, and CNT-CNT, respectively. At least five cells were made for each of the four CA combinations. Detailed property measurements for the dual-layered NCA cathodes are listed in Table S1. Electrodes with similar active material loadings, thicknesses, and compaction densities were obtained. The negative electrodes were made of 90 wt% artificial graphite (Shenzhen Kingrunning Energy Materials Co., Ltd., China), 5 wt% SP, 2 wt% carboxymethyl cellulose

(CMC, Cekol Servis LLC, Ukraine), and 3 wt% styrene butadiene rubber (SBR, Dow Chemical, USA). A relatively low compaction density of 1.6 g/cm³ was adopted in the anode to ensure that it would not be the limiting factor for cell performance. The capacity ratio of negative to positive electrodes was about 1.02.

Single-layer pouch cells were assembled in a dry room maintained at a ≤ -20 °C dew point and using cathode dimensions of 5.8 × 10.8 cm² and anode dimensions of 6.2 × 11.2 cm², and separated by Celgard 2325 (PP/PE/PP tri-layer membrane) separator. The cells were dried overnight at 80 °C under vacuum prior to electrolyte injection. Electrolyte composed of 1.2M LiPF₆ dissolved in ethylene carbonate (EC)/fluoroethylene carbonate (FEC)/ethyl methyl carbonate (EMC)/dimethyl carbonate (DMC) (3:1:2:4 by weight), with 1 wt% lithium difluoro(oxalate)borate (LiDFOB) as additive which may passivate the electrode/electrolyte interface by generating an CEI [28], was injected into the cells in an argon-filled glovebox with O₂ and H₂O content < 0.1 ppm.

Formation and electrochemical tests

Electrochemical performance of the pouch cells were tested on a LAND test device (CT2001B-5V-1A13, Land Instruments, China) at room temperature. All cells went through a formation process utilizing a 0.05 C rate after a 12-h initial stand period for electrolyte infiltration. Following cycles were performed at a 0.2 C rate. Both the formation and cycling processes utilized the following protocol: constant current (CC) charge to the cutoff voltage (4.25 V) immediately followed by a constant voltage (CV) mode until the current dropped to 0.01 C, then rest for 10 min, followed by a CC discharge to a cutoff voltage of 2.75 V. The respective C rates were based on the theoretical capacity of NCA, 1 C = 190 mA/g. Electrochemical impedance spectra (EIS) tests were performed using a CHI660E electrochemical workstation (Shanghai Chenhua Instrument Co., Ltd., China) in the frequency range of 0.01–100,000 Hz at different stages during the cells’ test processes in discharged state.

Characterization

The morphologies of the electrodes were characterized by scanning electron microscope (SEM, Hitachi, SU8020, Japan). Porosities of the electrodes were calculated by Eq. (1) [29]

$$P_c (\%) = \frac{V - W \left\{ \frac{C_{NCA}}{\rho_{NCA}} + \frac{C_{CA}}{\rho_{CA}} + \frac{C_{PVDF}}{\rho_{PVDF}} \right\}}{V} \times 100 \quad (1)$$

where P_c stands for porosity obtained by calculation; V is the volume of the electrode without current collector; C is the

mass ratio of NCA, CA, and PVDF in the electrode; ρ stands for the density of each component; and W represents the mass loading of the electrode. Raman spectra of conductive agents were obtained by an inVia Raman microscope (Renishaw, inVia, England). BET specific surface area was determined from N₂ adsorption using a Micromeritics ASAP 2460. Conductivities of the electrodes were measured using a four-point probe. X-ray photoelectron spectroscopy (XPS) data was acquired using an ESCALAB 250 Xi equipment (Thermo Fisher Scientific, USA).

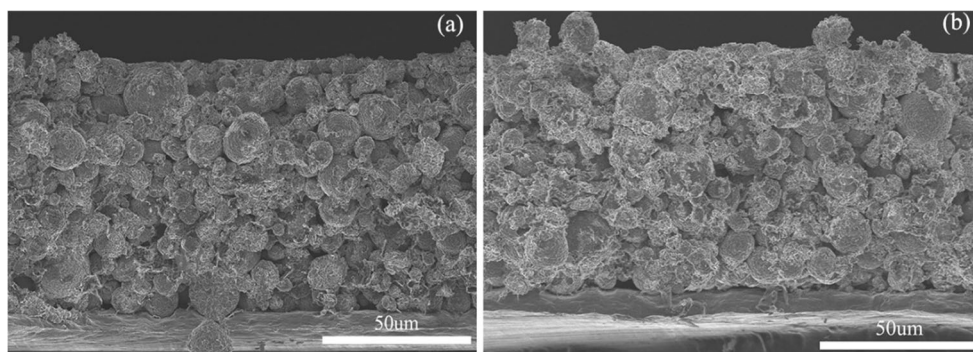
Results and discussion

SP and CNTs were chosen based on their ability to provide different types of electron conduction pathways, i.e., point-point and point-line [26]. These CAs may also regulate the fundamental porosity of the electrode based on various characteristics, such as aspect ratio (length/diameter) and specific area. The SEM images and BET test results shown in Figs. S1 and S2 illustrated some of the differences between the two CA types. It could be seen that CNTs have a diameter of about 15 nm and a length of 1–10 μm, which endowed it with a quite high aspect ratio, while the specific area of CNTs adopted in this work was 151.94 m²/g (determined by BET). In contrast, most SP particles were sphere- or granule-shaped, with particle sizes ranging between 50 and 100 nm and with a specific area of 61.84 m²/g (determined by BET), which was about 40% of that for CNTs.

Figure S3 displays the Raman spectra of CNTs and SP. The characteristic peaks located around 1349 cm⁻¹, 1589 cm⁻¹, and 2690 cm⁻¹ corresponded to the D band, G band, and 2D band, respectively [30]. An increasing intensity ratio of D band to G band (I_D/I_G) indicated that the structure of SP contained more defects [31], which should generally be expected to adversely affect its electrical conductivity. Moreover, the relatively higher intensity of the G band and the appearance of a 2D band in the CNT’s spectra implied that its graphitization degree and electronic conductivity would be expected to be higher than those of SP, and thus might potentially contribute to faster electron transport speed in the electrode [32].

Figures 1 and S4 show the cross sections and surface morphologies of the dual-layered electrodes. No aggregation was found either on the surfaces or in the cross sections, indicating that the CAs were evenly dispersed in the electrode. Total thickness of the coating layer was about 80 μm, and neither a separation nor a visible interface could be detected, which indicated that the upper layer was in intimate contact with the lower layer. Electrical conductivity of the electrodes was 0.02, 0.1, 0.1, and 0.2 S/cm, for SP-SP, CNT-SP, SP-CNT, and CNT-CNT, respectively, as obtained by the four-point probe. The CNT-CNT cathode demonstrated the highest

Fig. 1 Cross-sectional SEM images of SP-SP (a) and CNT-SP (b)



conductivity, at a value of approximately 10 times higher than that for the SP-SP cathode, and the coating sequence showed little influence on the electron transport as the CNT-SP and SP-CNT electrodes exhibited nearly equal conductivity values. The high conductivity of the CNT-containing electrode was attributed to both the larger surface area and the higher intrinsic conductivity of CNTs in comparison with that of SP. Aided by the high-speed mixing process, CNTs could be evenly dispersed on the cathode material surface and provided an interconnected electron transport network, so that better transport properties were obtained. At the same time, the higher surface area of the CNTs may provide higher electrode porosity. Applying Eq. 1 (P_c) and the image processing treatment (P_{ip}), porosity results were obtained as summarized in Table S2. Figure 2 illustrates the image processing (IP) treatment applied to the electrodes' cross-sectional SEM images through the ImagePro software[33]. P_{ip} and P_c were quite similar, which demonstrated the feasibility of the IP method. Considering that the electrode was prepared by a two-step coating method, we further separated the porosity distribution along the thickness direction into upper and lower parts via IP and the results are listed in Table S2. Figure 3 shows the results obtained by both calculation and image processing. It can be seen that the mean porosity obtained by IP method (mean of upper and lower porosity) was in accordance with that obtained via calculation. All the electrodes exhibited a gradient porosity distribution, with the upper layer being less porous than the lower layer. SP-SP and CNT-CNT electrodes exhibited the lowest (20.14%) and highest (23.83%) P_{ip} values, respectively, due to their differing surface areas and aspect ratios. Electrodes with CNTs in the lower layer showed higher slope in porosity as compared with that of the electrodes with SP in the lower layer, while all electrodes with

SP in the upper layer demonstrated lower overall porosity. All the 4 electrodes we prepared in this work showed high porosity in the lower layer. While, due to the different aspect ratio as well as surface area of CNT and SP, the rheological property of the as-prepared slurries was different (Fig. S5e), in which the one with CNT shows higher viscosity especially under low shear rate (just like in the coating process). Besides as shown in Fig. S5, the SP layer had more distinct porosity, which was beneficial for slurry permeation compared with the CNT layer. Therefore, when SP was used as the first layer, both CNT and SP slurry could penetrate into the pores and reduced the porosity in lower layer, which finally rendered lower porosity slope in the dual-layer electrode. On the contrary, when CNT was used as the first layer, it not only created higher porosity, but the slurry in the second layer could not infiltrate into its pore; therefore, higher porosity and larger slope was obtained.

Formation process and cycling data are shown in Fig. 4a. As for the formation process, all cathodes delivered quite similar initial specific capacity of 175.9~180.7 mAh/g (based on the weight of NCA), with SP-CNT showing the lowest (175.9 mAh/g) value and CNT-SP showing the highest (180.7 mAh/g). Initial coulombic efficiency (ICE) in the first formation cycle ranged from 81.21 to 84.24% (Fig. 4b), with the CNT-SP electrode demonstrating the highest value (84.24%). All the cells showed capacity improvement in the second formation cycle, most likely due to the gradually increasing electrolyte infiltration, the capacity then dropping as the C rate increased to 0.2 C. Cycle performance of the dual-layered electrodes was tested at room temperature, 0.2 C rate following the formation process without a post-formation degas and reseat step process. Interestingly, it was still the SP-CNT and CNT-SP electrode that exhibited the most (10.5 mAh/g) and least (4.2 mAh/g) capacity loss comparing the first cycle with the

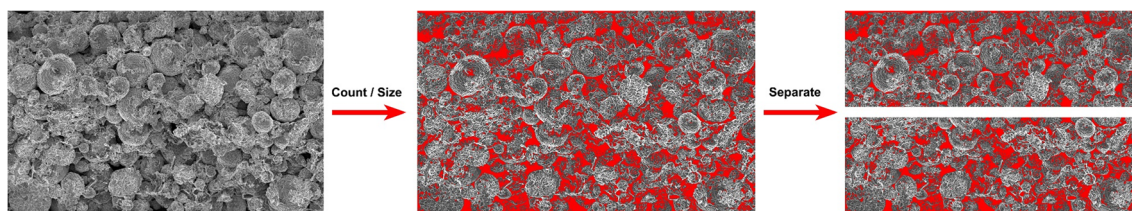


Fig. 2 Image processing through ImagePro software

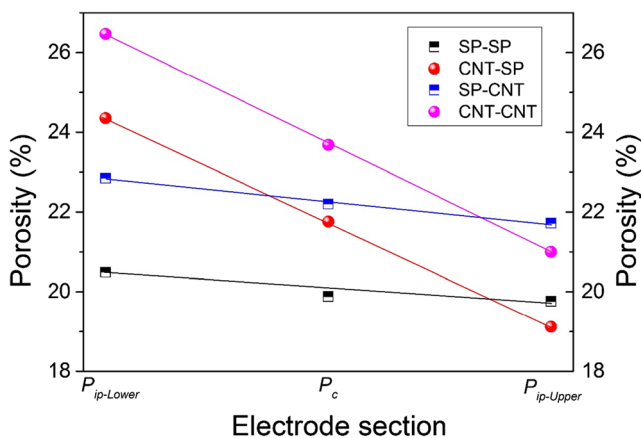


Fig. 3 Porosity distribution along the thickness direction of various electrodes

last formation, respectively. Considering that the two kinds of electrodes showed quite similar electronic conductivity as mentioned before, we inferred that it was Li^+ diffusion that influenced the capacity delivery here, and this deduction was verified by the EIS testing results (Fig. S6b). It can be seen that the bulk resistance (R_b) in the high frequency region contributed a major portion of the overall cell resistance (more than 40%), which may had a significant influence on the electrochemical performances of the cell. Although quite similar, while it can be noted that the CNT-SP cell exhibited a smaller R_b than that of the SP-CNT cell, even it was the SP-CNT electrode that has the higher mean and upper layer porosity. Specific discharge capacity of the cell with the CNT-SP electrode in the first 0.2 C cycle (after formation) was 177.5 mAh/g, which was the highest among the electrodes. It also demonstrated high capacity retention of 99.5% over 100 cycles, indicating that a stable interface film was formed in the formation process with the lowest level of parasitic reactions and/or active lithium consumption. It was found that all cells exhibited some capacity enhancement in the initial cycles, likely due to the electrolyte infiltration and activation processes, and among which the capacity increase for the CNT-CNT was low

due to its relatively higher porosity. Interestingly, it took a relatively shorter time for the cell with the SP-SP electrode to reach stable cycling, even though the electrode had the lowest porosity. This might be due to the low electric conductivity as previously described, and the high ionic and electronic resistance hindered the cell from delivering higher capacity. Moreover, it was noticed that both batteries using electrodes with CNT in the lower layer showed higher specific capacity than those with SP in the lower layer, apparently due to lower interfacial impedance between the coating and current collector[34]. The rate performance is shown in Fig. S6c. In order to observe and compare conveniently, all capacities of electrodes were normalized based on their capacity at 0.1 C, respectively. Though CNT-SP showed lower capacity at 0.2 and 0.5 C than CNT-CNT, which might be due to the higher conductivity of CNT-CNT, CNT-SP revealed superior performance when the current density increased to 1 C. Besides, CNT-SP showed the smallest variation among all the electrodes in the rate measurement from 0.1 to 1 C. Differential capacity versus voltage (dQ/dV) of electrodes after 100 cycles (the charge process) are shown in Fig. S6d. We could see that the peak positions were quite similar, which was in accordance with the limited capacity loss in the 100 cycles. While, the peaks of CNT-SP at about 3.5 and 3.65 V were higher than others, indicating a better lithium storage capability of CNT-SP. All electrochemical performance data are summarized in Table S3. We further calculated the energy density of each cathode by Eq. S1 [35], and the data are shown in Table S4, among which the CNT-SP cathode (557.98 Wh/kg) shows the highest energy density on electrode level.

CNT-SP and SP-SP were selected for further investigation to evaluate how the conductive networks impacted performance. They were initially studied using EIS to identify how the distribution of CA in two layers affected the resistance of cells. The Nyquist plots were simulated by ZsimpWin software according to the equivalent circuit insert in Fig. 5a, and the fitting data are given in Table 1. As shown in Fig. 5a and b, both EIS plots were composed of two partially overlapping

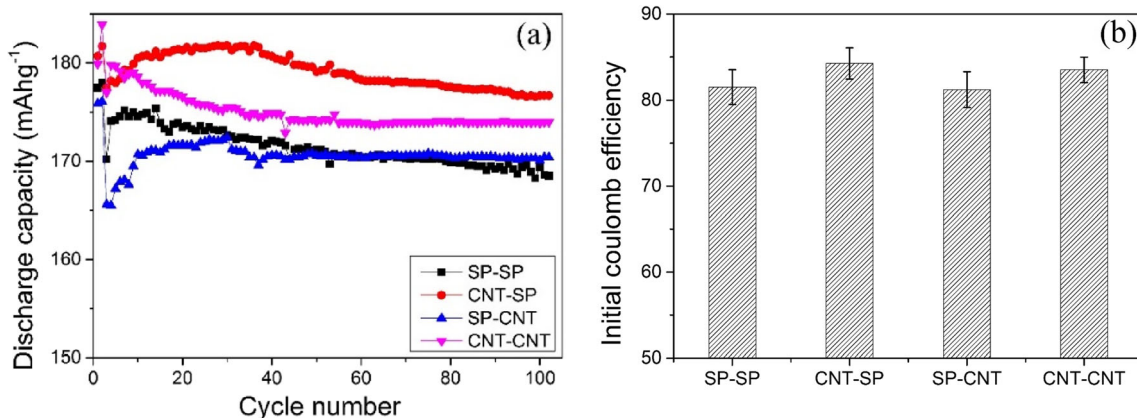


Fig. 4 Electrochemical performance of the pouch cells at 0.2 C: cycle performance (a) and initial coulomb efficiency of the first formation cycle (b)

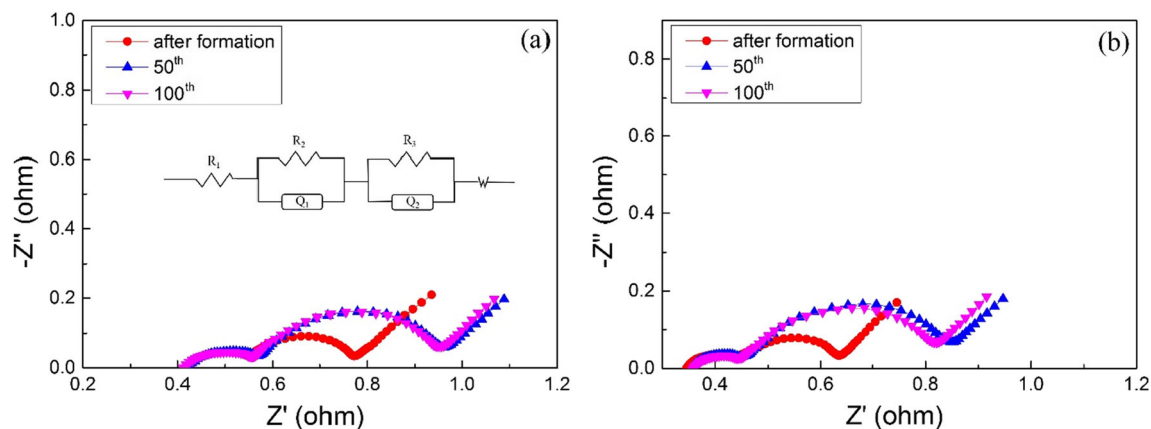


Fig. 5 EIS plots after different cycles of SP-SP (a) and CNT-SP (b)

semicircles and a sloping line. The cross points with the real axis in the high frequency region indicate the bulk or electrolyte resistance [36]. The first semicircle at high frequencies could be attributed to the resistance of the solid electrolyte interface (R_f), and the second one at medium to low frequency is associated with the charge transfer resistance (R_{ct}) [37, 38]. Based on the simulation results shown in Table 1, it was clear that R_b and R_{ct} dominate the cell resistance, which was aligned with other reports regarding thick electrodes [39, 40]. The R_b for CNT-SP was always smaller than that for SP-SP, indicating that the electrolyte infiltration in CNT-SP electrode was boosted by the optimized channel structure, which is in favor of enhanced capacity delivery. It was noteworthy that CNT-SP also showed a smaller R_f , which indicated that the cathode with better ionic and electron conductivity might facilitate the formation of a thinner CEI film. Both electrodes showed similar R_{ct} values that changed little at the 50th to 100th cycles, in concert with the cycling capacity data, which also indicates that the porosity or pore structures in this work have little influence on charge transfer. Figure 6 illustrates the morphology of the CNT-SP and SP-SP electrodes after 100 cycles. Some cracks were generated in the secondary particles of SP-SP, whereas the grain structure of CNT-SP appeared to be maintained. Furthermore, some fissures also appeared in the primary particles of SP-SP, likely causing the decline in reversible capacity and augmentation of side reactions. The SEM images of anodes are shown in Fig. S7, and no cracking could be observed, indicating that the structural integrity of graphite electrodes was maintained over 100 cycles. The

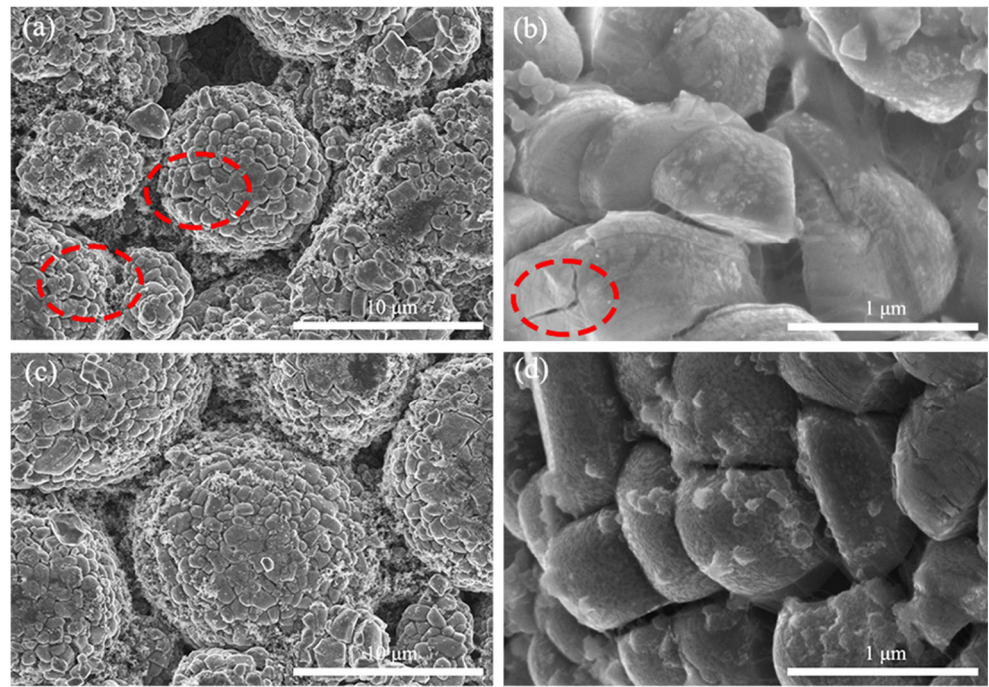
morphology of the anode cycled with the CNT-SP cathode was quite uniform. However, the anode cycled with the SP-SP cathode displayed dark areas (attributable to local lithiation differences), which indicates poor stability of the SEI layer in those areas.

XPS analyses of the cells with CNT-SP and SP-SP cathodes after 100 cycles were carried out to understand surface behavior of the NCA cathodes (Fig. 7). The C1s spectrum displayed a narrow main peak at 284.8 eV (C–C), which was assigned to carbon black (conductive ingredient of the electrode). Other peaks at 285.8 eV (C–H) and 290.7 eV (C–F) were attributed to the PVDF binder. The two remaining peaks at 286.3 eV (C–O) and 288.7 eV (C=O) belong to carbonates (LiCO_3 and ROCO_2Li) [41] resulting from the degradation of the electrolyte solvent, where the intensity of the SP-SP cathode was slightly greater than those of the CNT-SP cathode, which indicated a higher level of parasitic reactions with electrolyte. As for O 1s spectra, the peak at 529.4 eV is associated with metallic oxides, such as the NCA material. Other peaks at higher binding energy (531–535 eV) were attributed to oxygenated species [42]. By comparing the peak intensity of oxidation products, we concluded that more side reactions occurred at the surface of the SP-SP cathode. The peak at 687.5 eV ($\text{Li}_x\text{PO}_y\text{F}_z$ or Li_xPF_y) in the F 1s spectrum of the CNT-SP cathode was notably lower than that of the SP-SP cathode, indicating that much less LiPF_6 was decomposed on the CNT-SP cathode surface. Moreover, Fig. S8 shows that the $\text{Li}_x\text{PO}_y\text{F}_z$ content of SP-SP was lower than CNT-CNT, indicating that the upper layer

Table 1 Impedance of each component of SP-SP and CNT-SP after different cycles

Component	After formation(Ω)		After 50 cycle (Ω)		After100 cycle (Ω)	
	SP-SP	SP-SP	SP-SP	CNT-SP	SP-SP	CNT-SP
Bulk resistance (R_b)	0.427	0.348	0.424	0.357	0.415	0.360
Interface resistance (R_f)	0.132	0.108	0.162	0.109	0.158	0.100
Charge transfer resistance (R_{ct})	0.179	0.146	0.327	0.332	0.327	0.307

Fig. 6 SEM images of the SP-SP (a, b) and CNT-SP (c, d) after 100 cycles



with SP was helpful in the formation of thinner layer. Nevertheless, the Ni^{2+} (857.80 eV) and Ni^{3+} (860.41 eV) content of the CNT-SP cathode in the Ni 2p spectrum was similar

to that of the SP-SP cathode, which was in concert with the high capacity retention in both cells [43, 44]. The C 1s, O 1s, F 1s Li 1s, and Ni 2p spectra of the anodes are shown in Fig. S9.

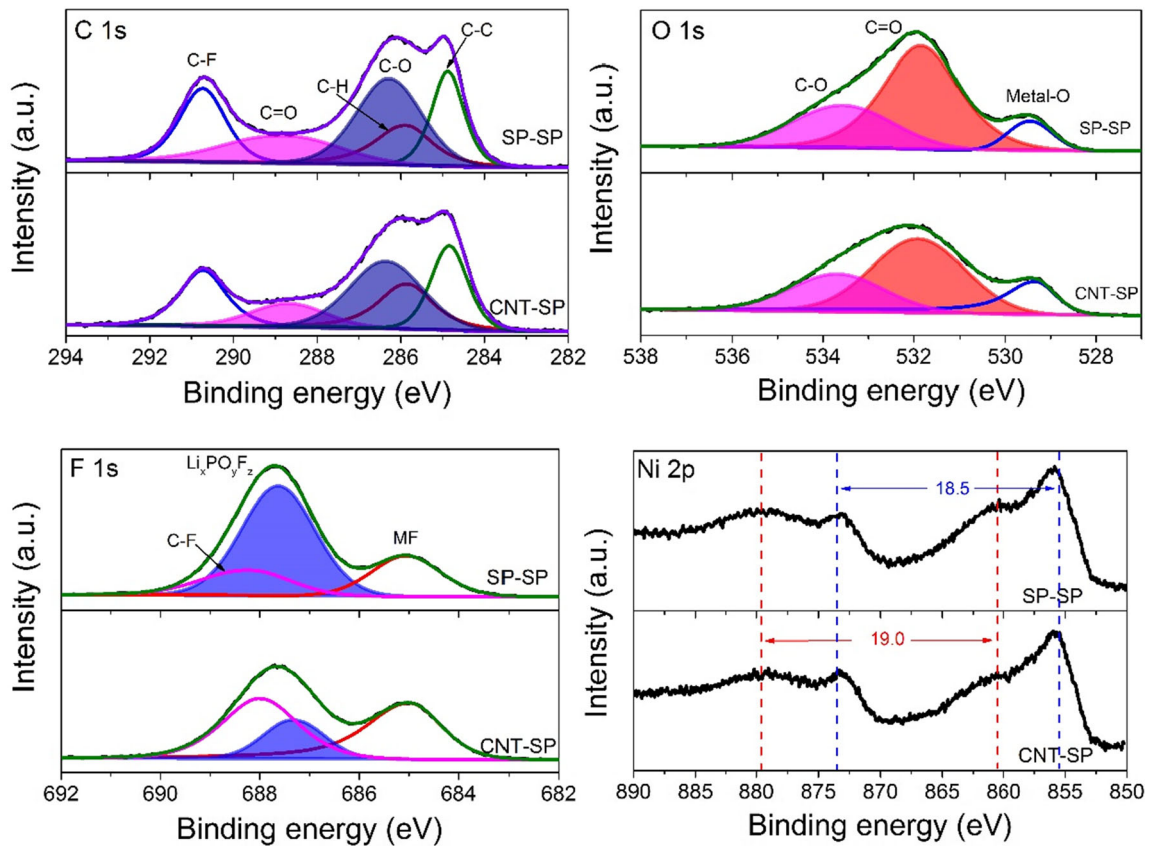
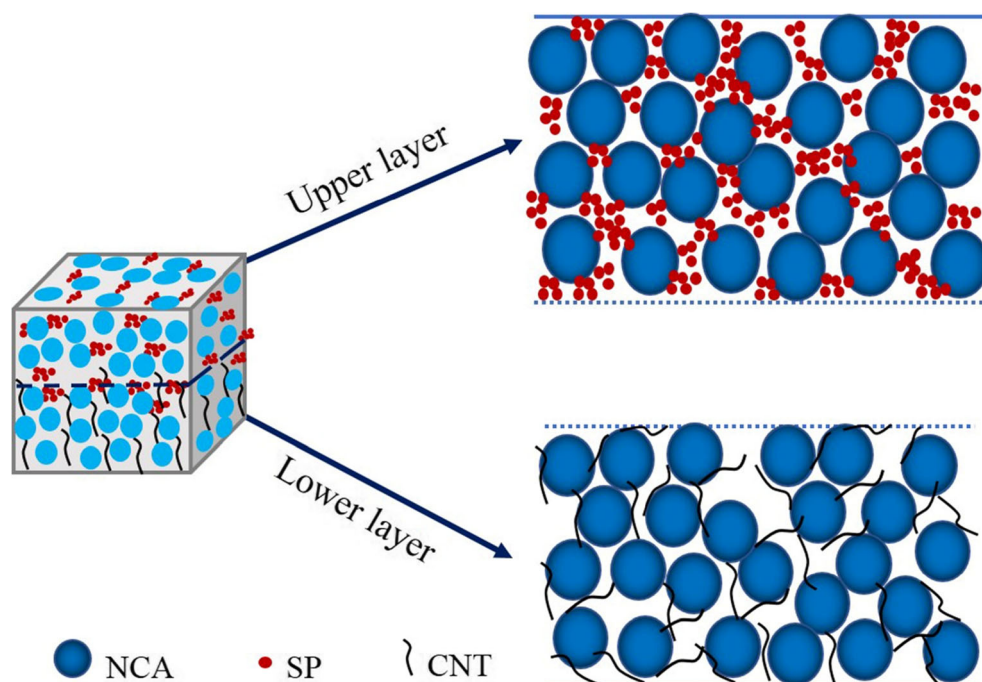


Fig. 7 XPS spectra of C 1s, O 1s, F 1s, and Ni 2p of cathodes of SP-SP and CNT-SP after 100 cycles

Fig. 8 Schematic diagrams of the dual-layered CNT-SP cathode



No significant differences were observed in C 1s and O1s spectra between anodes from the CNT-SP and SP-SP cathode cells. We found that one peak appeared at 685.12 eV in the F 1s spectrum, which could be recognized as MF (LiF or NiF₂), and this was confirmed by the Li 1s and Ni 2p spectra. More LiF deposited on the anode surface (in the CNT-SP cathode cell) can contribute to the stability and uniformity of the SEI film [45], which was also in agreement with the SEM images (Fig. S7). The discovery of Ni²⁺ demonstrated that transition metal dissolution and penetration may have contributed to the capacity loss [46]. Obviously, the peak density is much less in CNT-SP, which further supported its enhanced cycle stability.

In summary, a thick CNT-SP electrode with areal capacity of about 5 mAh/cm² and reasonable porosity for Li⁺ diffusion was created. This method can allow for accelerated electrolyte infiltration, diminished polarization, and greater deterioration protection for the NCA cathode. Figure 8 illustrates the more ideal cathode structure as obtained in this study. SP with lower surface area in the upper layer (close to the separator) will help decrease the electrode porosity and side reaction. A thinner CEI film is formed on the surface of the NCA particles, and less lithium will be irreversibly consumed with this electrode configuration. In terms of the lower layer (close to the current collector), the higher conductivity of the CNTs not only decreases the interface impedance between the current collector and electrode coating but also benefits the long-distance ion transport by increasing the apparent electrode porosity. The synergistic effect of SP and CNTs can accelerate both Li⁺ diffusion and electron conduction. This could enhance active material utilization, and therefore, cell performance was also improved in this CNT-SP cathode cell.

Conclusion

In this work, we have fabricated dual-layered NCA cathodes with different conductive agents to study the influence of the gradient porosity and conductivity contribution on the electrochemical behaviors of full pouch cells. We find that CNT-SP cathode-based cells exhibit better performance with 4.81 mAh/cm² areal capacity and 99.5% capacity retention after 100 cycles at 0.2 C, due to the superior conductive network configuration. The CNTs, with their higher conductivity and larger surface area utilized in the lower layer (close to the current collector), can reduce the interfacial impedance and accelerate electrolyte infiltration. The SP in the upper layer (close to the separator) provides reasonable porosity while also increasing NCA stability. The nature of the porosity induced in this implementation of these two CAs is beneficial to the Li⁺ diffusion. In addition, the 3D network of the CNT-SP electrode provides increased protection of the NCA particles from degradation. This method offers an effective approach to beneficially alter the performance of thick electrodes and improve active material utilization.

Supplementary Information The online version contains supplementary material available at <https://doi.org/10.1007/s11581-021-03912-6>.

Funding This work was supported by the National Key Research and Development Program of China (No. 2019YFA0705600), the National Natural Science Foundation of China (No.21706261 and No. 21706262), the Henan province science and technology cooperation project (182106000022) and the Ford University Research Program.

References

- Kang K, Meng YS (2006) Electrodes with high power and high capacity for rechargeable lithium batteries. *Science* 311:977–980
- Kim T-H, Park J-S, Chang SK, Choi S, Ryu JH, Song H-K (2012) The current move of lithium ion batteries towards the next phase. *Adv Energy Mater* 2:860–872
- Whittingham MS (2004) Lithium batteries and cathode materials. *Chem Rev* 104:4271–4302
- Goodenough JB (2013) Evolution of strategies for modern rechargeable batteries. *Acc Chem Res* 46:1053–1061
- Manthiram A (2017) An outlook on lithium ion battery technology. *ACS Central Sci* 3:1063–1069
- Zeng X, Li M, Abd El-Hady D, Alshitari W, Al-Bogami AS, Lu J, Amine K (2019) Commercialization of lithium battery technologies for electric vehicles. *Adv Energy Mater* 9:1900161
- Kuang Y, Chen C, Pastel G, Li Y, Song J, Mi R, Kong W, Liu B, Jiang Y, Yang K, Hu L (2018) Conductive cellulose nanofiber enabled thick electrode for compact and flexible energy storage devices. *Adv Energy Mater* 8:1802398
- Lu LL, Lu YY, Xiao ZJ, Zhang TW, Zhou F, Ma T, Ni Y, Yao HB, Yu SH, Cui Y (2018) Wood-inspired high-performance ultrathick bulk battery electrodes. *Adv Mater* 30:1706745
- Wang JS, Liu P, Sherman E, Verbrugge M, Tataria H (2011) Formulation and characterization of ultra-thick electrodes for high energy lithium-ion batteries employing tailored metal foams. *J Power Sources* 196:8714–8718
- Xia Y, Mathis TS, Zhao MQ, Anasori B, Dang A, Zhou Z, Cho H, Gogotsi Y, Yang S (2018) Thickness-independent capacitance of vertically aligned liquid-crystalline MXenes. *Nature* 557:409–412
- Singh M, Kaiser J, Hahn H (2015) Thick electrodes for high energy lithium ion batteries. *J Electrochem Soc* 162:A1196–A1201
- Danner T, Singh M, Hein S, Kaiser J, Hahn H, Latz A (2016) Thick electrodes for Li-ion batteries: a model based analysis. *J Power Sources* 334:191–201
- Singh M, Kaiser J, Hahn H (2016) A systematic study of thick electrodes for high energy lithium ion batteries. *J Electroanal Chem* 782:245–249
- Gao H, Wu Q, Hu Y, Zheng JP, Amine K, Chen Z (2018) Revealing the rate-limiting Li-ion diffusion pathway in ultrathick electrodes for Li-ion batteries. *J Phys Chem Lett* 9:5100–5104
- Evanoff K, Khan J, Balandin AA, Magasinski A, Ready WJ, Fuller TF, Yushin G (2012) Towards ultrathick battery electrodes: aligned carbon nanotube-enabled architecture. *Adv Mater* 24:533–537
- Newman J (1995) Optimization of porosity and thickness of a battery electrode by means of a reaction-zone model. *J Electrochem Soc* 142:97–101
- Lopez J, Chen Z, Wang C, Andrews SC, Cui Y, Bao Z (2016) The effects of cross-linking in a supramolecular binder on cycle life in silicon microparticle anodes. *ACS Appl Mater Interfaces* 8:2318–2324
- Srinivasan V, Newman J (2004) Design and optimization of a natural graphite/iron phosphate lithium-ion cell. *J Electrochem Soc* 151:A1530
- Yu S, Kim S, Kim TY, Nam JH, Cho WI (2012) Transportation properties in nanosized LiFePO₄ positive electrodes and their effects on the cell performance. *J Appl Electrochem* 43:253–262
- Strobridge FC, Orvananos B, Croft M, Yu H-C, Robert R, Liu H, Zhong Z, Connolley T, Drakopoulos M, Thornton K, Grey CP (2015) Mapping the inhomogeneous electrochemical reaction through porous LiFePO₄ electrodes in a standard coin cell battery. *Chem Mater* 27:2374–2386
- Bae CJ, Erdonmez CK, Halloran JW, Chiang YM (2013) Design of battery electrodes with dual-scale porosity to minimize tortuosity and maximize performance. *Adv Mater* 25:1254–1258
- Chen L-C, Liu D, Liu T-J, Tiu C, Yang C-R, Chu W-B, Wan C-C (2016) Improvement of lithium-ion battery performance using a two-layered cathode by simultaneous slot-die coating. *J Energy Storage* 5:156–162
- Du Z, Wood DL, Daniel C, Kalnaus S, Li J (2017) Understanding limiting factors in thick electrode performance as applied to high energy density Li-ion batteries. *J Appl Electrochem* 47:405–415
- Xu J, Zhang L, Wang Y, Chen T, Al-Shroofy M, Cheng YT (2017) Unveiling the critical role of polymeric binders for silicon negative electrodes in lithium-ion full cells. *ACS Appl Mater Interfaces* 9:3562–3569
- Wang Z, Lee JZ, Xin HL, Han L, Grillon N, Guy-Bouyssou D, Bouyssou E, Proust M, Meng YS (2016) Effects of cathode electrolyte interfacial (CEI) layer on long term cycling of all-solid-state thin-film batteries. *J Power Sources* 324:342–348
- Betz J, Brinkmann JP, Nölle R, Lürenbaum C, Kolek M, Stan MC, Winter M, Placke T (2019) Cross talk between transition metal cathode and li metal anode: unraveling its influence on the deposition/dissolution behavior and morphology of lithium. *Adv Energy Mater* 9:1900574
- Wang J, Shen Z, Yi M (2019) Liquid-exfoliated graphene as highly efficient conductive additives for cathodes in lithium ion batteries. *Carbon* 153:156–163
- Haregewoin AM, Wotango AS, Hwang BJ (2016) Electrolyte additives for lithium ion battery electrodes: progress and perspectives. *Energy Environ Sci* 9:1955–1988
- Park J, Hyeon S, Jeong S, Kim H-J (2019) Performance enhancement of Li-ion battery by laser structuring of thick electrode with low porosity. *J Ind Eng Chem* 70:178–185
- Du Z, Li J, Wood M, Mao C, Daniel C, Wood DL (2018) Three-dimensional conductive network formed by carbon nanotubes in aqueous processed NMC electrode. *Electrochim Acta* 270:54–61
- Ren W, Wang K, Yang J, Tan R, Hu J, Guo H, Duan Y, Zheng J, Lin Y, Pan F (2016) Soft-contact conductive carbon enabling depolarization of LiFePO₄ cathodes to enhance both capacity and rate performances of lithium ion batteries. *J Power Sources* 331:232–239
- Su X, Ha S, Ishwait MB, Lei HW, Oljaca M, Blizanac B, Dees D, Lua WQ (2016) Nonlinear conductivities and electrochemical performances of LiNi_{0.5}Co_{0.2}Mn_{0.3}O₂ electrodes. *J Electrochem Soc* 163:A2720–A2724
- Lin Liu PG, Liu C (2017) Experimental and simulation investigations of porosity graded cathodes in mitigating battery degradation of high voltage lithium-ion batteries. *J Electrochem Soc* 164:A3163–A3173
- Liu T, Li X, Sun S, Sun X, Cao F, Ohsaka T, Wu J (2018) Analysis of the relationship between vertical impurity distribution of conductive additive and electrochemical behaviors in lithium ion batteries. *Electrochim Acta* 269:422–428
- Agostini M, Hwang J-Y, Kim HM, Bruni P, Brutti S, Croce F, Matic A, Sun Y-K (2018) Minimizing the electrolyte volume in Li-S batteries: a step forward to high gravimetric energy density. *Adv Energy Mater* 8:1801560
- Osaka T, Momma T, Mukoyama D, Nara H (2012) Proposal of novel equivalent circuit for electrochemical impedance analysis of commercially available lithium ion battery. *J Power Sources* 205:483–486
- Maheshwari A, Heck M, Santarelli M (2018) Cycle aging studies of lithium nickel manganese cobalt oxide-based batteries using electrochemical impedance spectroscopy. *Electrochim Acta* 273:335–348
- Zhang Y, Wang C-Y (2009) Cycle-life characterization of automotive lithium-ion batteries with LiNiO₂ cathode. *J Electrochem Soc* 156:A527–A535
- Ogihara N, Kawauchi S, Okuda C, Itou Y, Takeuchi Y, Ukyo Y (2012) Theoretical and experimental analysis of porous electrodes

- for lithium-ion batteries by electrochemical impedance spectroscopy using a symmetric cell. *J Electrochem Soc* 159:A1034–A1039
40. Hu L, La Mantia F, Wu H, Xie X, McDonough J, Pasta M, Cui Y (2011) Lithium-ion textile batteries with large areal mass loading. *Adv Energy Mater* 1:1012–1017
 41. Liu C, Qian K, Lei D, Li B, Kang F, He Y-B (2018) Deterioration mechanism of $\text{LiNi}_0.8\text{Co}_0.15\text{Al}_0.05\text{O}_2/\text{graphite-SiO}_x$ power batteries under high temperature and discharge cycling conditions. *J Mater Chem A* 6:65–72
 42. Bodenes L, Dedryvere R, Martinez H, Fischer F, Tessier C, Peres JP (2012) Lithium-ion batteries working at 85 degrees C: aging phenomena and electrode/electrolyte interfaces studied by XPS. *J Electrochem Soc* 159:A1739–A1746
 43. Tao Chen FW, Lia X, Yan X, Wang H, Deng B, Xie Z, Qu M (2019) Dual functional MgHPO_4 surface modifier used to repair deteriorated NiRich $\text{LiNi}_0.8\text{Co}_0.15\text{Al}_0.05\text{O}_2$ cathode material. *Appl Surf Sci* 465:863–870
 44. Hou P, Zhang H, Deng X, Xu X, Zhang L (2017) Stabilizing the electrode/electrolyte interface of $\text{LiNi}_0.8\text{Co}_0.15\text{Al}_0.05\text{O}_2$ through tailoring aluminum distribution in microspheres as long-life, high-rate, and safe cathode for lithium-ion batteries. *ACS Appl Mater Interfaces* 9:29643–29653
 45. De Juan LMZ, Maggay IVB, Nguyen MT, Liu W-R, Yonezawa T (2018) $\beta\text{-Sn}$ Nanorods with Active (001) Tip induced LiF-rich SEI layer for stable anode material in lithium ion battery. *ACS Appl Nano Mater* 1:3509–3519
 46. Chen Z, Zhang L, Wu X, Song K, Ren B, Li T, Zhang S (2019) Effect of N/P ratios on the performance of $\text{LiNi}_0.8\text{Co}_0.15\text{Al}_0.05\text{O}_2\|\text{SiO}_2/\text{Graphite}$ lithium-ion batteries. *J Power Sources* 439:227056

Publisher's note Springer Nature remains neutral with regard to jurisdictional claims in published maps and institutional affiliations.